A&A 646, A158 (2021)
https://doi.org/10.1051/0004-6361/202039511

Astronomy & Astrophysics

ESPRESSO high-resolution transmission spectroscopy of WASP-76 b*

H. M. Tabernero[1,2], M. R. Zapatero Osorio[2], R. Allart[3], F. Borsa[4], N. Casasayas-Barris[5,6], O. Demangeon[1,14], D. Ehrenreich[3], J. Lillo-Box[2], C. Lovis[3], E. Pallé[5,6], S. G. Sousa[1], R. Rebolo[5,6], N. C. Santos[1,14], F. Pepe[3], S. Cristiani[7], V. Adibekyan[1,14], C. Allende Prieto[5,6], Y. Alibert[8], S. C. C. Barros[1], F. Bouchy[3], V. Bourrier[3], V. D'Odorico[7], X. Dumusque[3], J. P. Faria[1,14], P. Figueira[9,1], R. Génova Santos[5,6], J. I. González Hernández[5,6], S. Hojjatpanah[1,14], G. Lo Curto[9], B. Lavie[3], C. J. A. P. Martins[1,16], J. H. C. Martins[1,14], A. Mehner[9], G. Micela[10], P. Molaro[7,15], N. J. Nunes[1,11], E. Poretti[4,12], J. V. Seidel[3], A. Sozzetti[13], A. Suárez Mascareño[5,6], S. Udry[3], M. Aliverti[4], M. Affolter[8], D. Alves[11], M. Amate[5,6], G. Avila[9], T. Bandy[8], W. Benz[8], A. Bianco[4], C. Broeg[8], A. Cabral[1,11], P. Conconi[4], J. Coelho[1,11], C. Cumani[9], S. Deiries[9], H. Dekker[9], B. Delabre[9], A. Fragoso[5,6], M. Genoni[4], L. Genolet[3], I. Hughes[3], J. Knudstrup[9], F. Kerber[9], M. Landoni[4], J. L. Lizon[9], C. Maire[3], A. Manescau[9], P. Di Marcantonio[7], D. Mégevand[3], M. Monteiro[1,14], M. Monteiro[1,11], M. Moschetti[4], E. Mueller[9], A. Modigliani[9], L. Oggioni[4], A. Oliveira[1,11], G. Pariani[4], L. Pasquini[9], J. L. Rasilla[5,6], E. Redaelli[4], M. Riva[4], S. Santana-Tschudi[5,6], P. Santin[7], P. Santos[1,11], A. Segovia[3], D. Sosnowska[3], P. Spanò[4], F. Tenegi[5,6], O. Iwert[9], A. Zanutta[4], and F. Zerbi[4]

(Affiliations can be found after the references)

Received 23 September 2020 / Accepted 22 November 2020

ABSTRACT

Aims. We report on ESPRESSO high-resolution transmission spectroscopic observations of two primary transits of the highly irradiated, ultra-hot Jupiter-sized planet, WASP-76b. We investigated the presence of several key atomic and molecular features of interest that may reveal the atmospheric properties of the planet.

Methods. We extracted two transmission spectra of WASP-76b with $R \approx 140\,000$ using a procedure that allowed us to process the full ESPRESSO wavelength range (3800–7880 Å) simultaneously. We observed that at a high signal-to-noise ratio, the continuum of ESPRESSO spectra shows 'wiggles', which are likely caused by an interference pattern outside the spectrograph. To search for the planetary features, we visually analysed the extracted transmission spectra and cross-correlated the observations against theoretical spectra of different atomic and molecular species.

Results. The following atomic features are detected: Li I, Na I, Mg I, Ca II, Mn I, K I, and Fe I. All are detected with a confidence level between 9.2 σ (Na I) and 2.8 σ (Mg I). We did not detect the following species: Ti I, Cr I, Ni I, TiO, VO, and ZrO. We impose the following 1 σ upper limits on their detectability: 60, 77, 122, 6, 8, and 8 ppm, respectively.

Conclusions. We report the detection of Li I on WASP-76b for the first time. In addition, we confirm the presence of Na I and Fe I as previously reported in the literature. We show that the procedure employed in this work can detect features down to the level of ~0.1% in the transmission spectrum and ~10 ppm by means of a cross-correlation method. We discuss the presence of neutral and singly ionised features in the atmosphere of WASP-76b.

Key words. planets and satellites: atmospheres – planets and satellites: individual: WASP-76b

1. Introduction

Planets orbiting late-type stars are ubiquitous, as demonstrated by the thousands of planets discovered to date[1]. Their numbers have been steadily increasing during the last decades thanks to multiple spectroscopic and photometric surveys carried out by, for example, the space missions *Kepler* (Borucki et al. 2010) and TESS (Ricker 2014), and the ground-based spectrographs HARPS (Mayor et al. 2003), HARPS-N (Cosentino et al. 2012), HIRES (Vogt et al. 1994), CARMENES (Quirrenbach et al. 2016), and MARVELS (Alam et al. 2015). Moreover, their numbers and our knowledge of exoplanets will increase thanks to new and future observing facilities like ESPRESSO (Pepe et al. 2010, 2021), CHEOPS (Rando et al. 2018), HPF (Mahadevan et al. 2014), JWST (Gardner et al. 2006), PLATO (Rauer et al. 2014), NIRPS (Wildi et al. 2017), and SPIRou (Moutou et al. 2015). Exoplanetary research is now approaching the deep study and characterisation of the atmospheres of the extrasolar planets.

It is of great interest to investigate transiting exoplanets and their atmospheres, and to learn about their bulk chemical compositions. In particular, highly irradiated gaseous planets are a key target for atmospheric characterisation due to their intrinsic properties, such as their proximity to the parent host star, their transit depth, and their transit duration. Charbonneau et al. (2002) reported the first detection of an exoplanet atmosphere by means of HST transmission spectroscopy. However, Casasayas-Barris et al. (2020, 2021) raised some doubts over that detection, showing that it could be explained by the Rossiter-McLaughlin

* Based on guaranteed time observations collected at the European Southern Observatory under ESO programme 1102.C-0744 by the ESPRESSO Consortium.

[1] https://exoplanetarchive.ipac.caltech.edu

effect. In spite of this, Charbonneau et al. (2002) opened a new era in the study of the atmospheres of transiting exoplanets. The first neutral sodium detection in HD 209458 b with a ground-based telescope was made by Snellen et al. (2008) as well as for HD 189733 b by Redfield et al. (2008). Several chemical species have already been reported in the atmospheres of tens of the so-called ultra-hot Jupiters (UHJs), which are giant gaseous planets with typical equilibrium temperatures (T_{eq}) above ≈2200 K (see Parmentier et al. 2018). In particular, Fe I,II and Ti I,II have been detected in the atmosphere of the UHJ Kelt-9 b (Hoeijmakers et al. 2018, 2019). In addition, Fe I,II has also been reported in other UHJs such as MASCARA-2b (Casasayas-Barris et al. 2019), WASP-121b (Gibson et al. 2020; Hoeijmakers et al. 2020), or WASP-76b (Ehrenreich et al. 2020). Other species such as He, Na, Mg, K, V, Cr, CO, CH_4, or water vapor have been reported in the atmospheres of tens of highly irradiated gaseous planets (e.g. Barman et al. 2015; Wyttenbach et al. 2015; Sheppard et al. 2017; Chen et al. 2018; Nortmann et al. 2018; Parmentier et al. 2018; Allart et al. 2018, 2019; Alonso-Floriano et al. 2019; Seidel et al. 2019; Hoeijmakers et al. 2020).

Spectroscopy is currently a powerful tool able to detect atomic or molecular features in the transmission spectra of transiting exoplanets, which in turn are key to revealing their internal chemistry and surface compositions. The Echelle Spectrograph for Rocky Exoplanets and Stable Spectroscopic Observations (ESPRESSO; see Pepe et al. 2010, 2021) is the new generation high-resolution spectrograph at the 8-m Very Large Telescope (VLT) at Paranal, Chile. ESPRESSO at the VLT offers an excellent opportunity for atmospheric characterisation, given the large collecting area of the VLT. This is a key factor for achieving the necessary signal-to-noise ratio (S/N) per resolution element during the critical and limited observational windows of transiting exoplanets. In addition, studying the atmospheres of gas giant planets at optical wavelengths is a complement to future observations at much longer wavelengths by JWST (Gardner et al. 2006) and Ariel (Tinetti et al. 2016).

In this work, we present the detailed analysis of the transmission spectrum of WASP-76b using ESPRESSO data. WASP-76b orbits an F7 V star with $m_V \approx 9.5$ mag with an orbital period of approximately 1.8 d (West et al. 2016; Ehrenreich et al. 2020). WASP-76b is an inflated UHJ with roughly one Jupiter mass and twice its radius with an equilibrium temperature of more than 2200 K. Thus, it is a perfect target for atmospheric characterisation given its high equilibrium temperature and the high-metallicity of the host-star (see Seidel et al. 2019; Ehrenreich et al. 2020; Edwards et al. 2020; von Essen et al. 2020). We analysed the same data as in Ehrenreich et al. (2020) with the objective of exploring which spectral atomic and molecular species can be detected using ESPRESSO.

This manuscript is organised into the following sections: the ESPRESSO observations are presented in Sect. 2; the extraction of the transmission spectrum is described in Sect. 3; while the stellar characterisation of WASP-76 can be found in Sect. 4; the transmission spectrum is analysed in Sect. 5; and finally, the summary and conclusions are given in Sect. 6.

2. Observational data

We collected several high-resolution *echelle* spectra covering two transits of the ultra-hot Jupiter, WASP-76b, using the HR21[2] mode of ESPRESSO covering the optical wavelengths from 3800 to 7880 Å with $R \approx 140\,000$. These two transit observations were carried out as part of the ESPRESSO Guaranteed Time Observations under ESO programme 1102.C-744. The observations were reduced using the ESPRESSO reduction pipeline[3]. The pipeline delivers the necessary products to further process the data; for example, barycentric corrected radial velocities (V_r), the stellar fluxes together with their uncertainties, wavelengths (in vacuum), and S/N.

The two transits of WASP-76b were observed on the following Universal Time (UT) dates: 2018 September 03 (first transit, hereafter T1) and 2018 October 31 (second transit, T2). On both occasions, we observed the target uninterruptedly for ∼2 h before, during, and ∼2 h after the transit. In T1, we collected a total of 36 ESPRESSO spectra with an individual exposure time of 600 s; in T2, we acquired 70 spectra of 300 s each. The average S/N of each individual observation is about 120 per pixel element at ∼5500 Å (see Ehrenreich et al. 2020). For T1, we performed longer exposure times than for T2 due to weather constraints (i.e. poor seeing). Unfortunately, the ESPRESSO atmospheric dispersion corrector (ADC) is not built to correct the atmospheric transmission above an airmass of 2.2. Thus, we discarded two spectra for both transits because they were not suitable for any meaningful transmission spectrum retrieval and later analysis. Other details regarding the observations for these two transits of WASP-76b can be found in Table 1, while information on the dates and radial velocities can be found in Ehrenreich et al. (2020).

Table 1. Summary of WASP-76b transit observations.

Date	Number of spectra			t_{exp} (s)
	Total	In-transit	Out-of-transit	
2018-09-03	36	20	16	600
2018-10-31	70	38	32	300

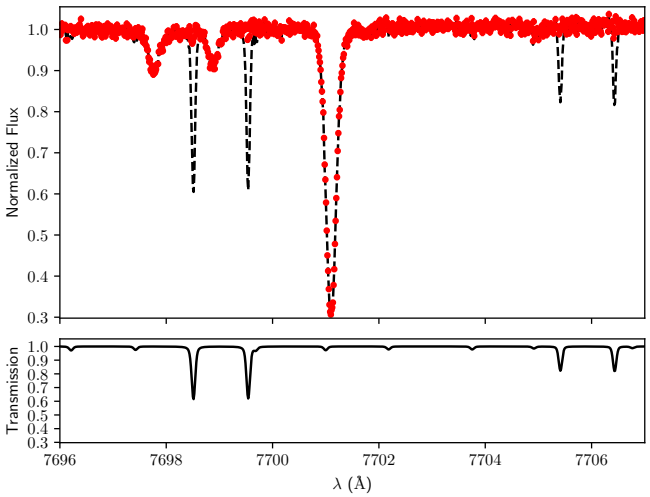

Fig. 1. Example of our telluric correction procedure in the K I region. *Top panel*: uncorrected spectrum (black dashed line) and corrected spectrum (red dots). *Bottom panel*: best telluric correction solution for a WASP-76 spectrum in this particular wavelength range.

[2] HR21 uses a binning of a factor of 2 in the direction perpendicular to wavelength.

[3] https://www.eso.org/sci/software/pipelines/

Table 2. `Molecfit` parameters used to correct telluric lines.

Parameter	Value	Description
`ftol`	10^{-5}	χ^2 tolerance
`xtol`	10^{-5}	Tolerance for the `molectfit` fitted variables
`fit_cont`	1	Continuum fitting flag
`cont_n`	3	Degree of polynomial continuum
`fit_res_gauss`	1	Gaussian kernel
`res_gauss`	3.5	Kernel size (pixels)
`kernfac`	6.0	Kernel size measured in units of the kernel $FWHM$
`list_molec`	H_2O,O_2	Molecules to be synthetised

Table 3. Orbital and physical parameters for the WASP-76 system.

Parameter	Value	Reference
	Stellar parameters	
$T_{\rm eff}$	6316 ± 64 K	This work
$\log g$	4.13 ± 0.14 dex	This work
[Fe/H]	0.34 ± 0.05 dex	This work
A(Li)	2.47 dex	This work
ξ	1.38 ± 0.07 km s^{-1}	This work
M_*	1.45 ± 0.02 $M_\odot$	This work
R_*	1.77 ± 0.07 $R_\odot$	This work
$m_{\rm V}$	9.5 mag	West et al. (2016)
π	5.12 ± 0.16 mas	Gaia Collaboration (2018)
d	195 ± 6 pc	Gaia Collaboration (2018)
	Planet parameters	
P	1.809886 ± 0.000001 d	Ehrenreich et al. (2020)
$M_{\rm p}$	0.92 ± 0.03 $M_{\rm J}$	Ehrenreich et al. (2020)
$R_{\rm p}$	1.83 ± 0.05 $R_{\rm J}$	Ehrenreich et al. (2020)
K_1	0.1193 ± 0.0018 km s^{-1}	Ehrenreich et al. (2020)
γ	−1.0733 ± 0.0002 km s^{-1}	Ehrenreich et al. (2020)
e	0	Assumed
ω	90	Assumed

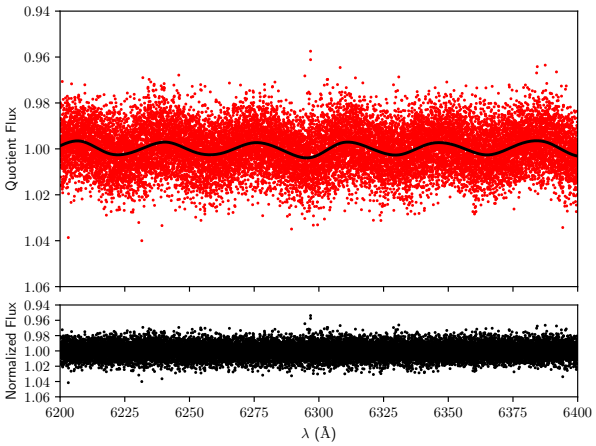

Fig. 2. Wiggle correction for a residual spectrum. *Upper panel*: original residuals (red) and the cubic splines used to fit the wiggles (black). *Lower panel*: final residual spectrum after removing the wiggles.

3. Data analysis

3.1. Telluric correction

The telluric lines have to be removed from the data before extracting the transmission spectrum of WASP-76b, as they might contaminate the final result. To that aim, we gathered the processed 1D sky-corrected spectra provided by the ESPRESSO reduction pipeline. We corrected for the telluric absorption lines by means of the `Molecfit`[4] software suite (Smette et al. 2015; Kausch et al. 2015). The spectra provided by the ESPRESSO pipeline were already corrected for the Barycentric Earth Radial Velocity (BERV). However, `Molecfit` models the telluric transmission spectrum in the terrestial reference frame (see, e.g.

Table 4. Chemical abundances relative to solar value ([X/H]) for WASP-76.

Species	[X/H] (dex)	$\sigma_{\rm lines}$ (dex)	$N_{\rm lines}$
C I	0.19	0.03	3
O I	0.21	0.01	3
Na I	0.48	0.05	4
Mg I	0.32	0.04	2
Si I	0.36	0.09	22
K I	0.39	–	1
Ca I	0.41	0.09	18
Ti I	0.35	0.06	18
Cr I	0.38	0.07	10
Mn I	0.32	0.01	3
Ni I	0.35	0.05	33

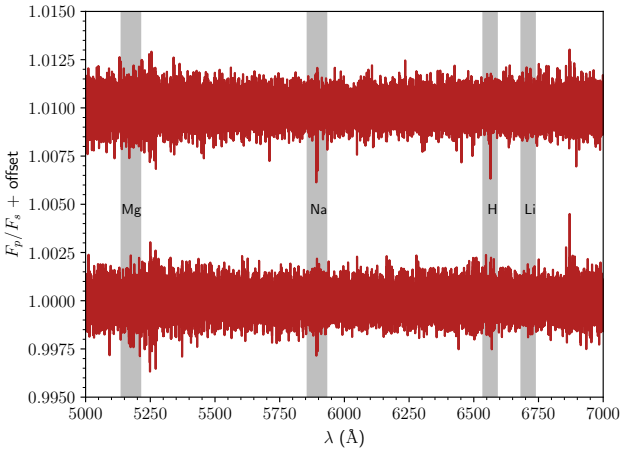

Fig. 3. Transmission spectra for WASP-76b in the 5000–7000 Å range: a few key features are shaded in grey. The T1 is the top spectrum and T2 is the bottom one. A binning of 0.1 Å has been applied to the data for clarity. All wavelengths are given in vacuum.

[4] https://www.eso.org/sci/software/pipelines/skytools/molecfit

Table 5. Properties of atomic lines studied in this work.

Line	λ [Å]	Transit	h [%]	$V_{\rm wind}$ [km s^{-1}]	$FWHM$ [km s^{-1}]	R_λ [$R_{\rm p}$]	Significance [σ]
Ca II K	3934.78	T1	1.75 ± 0.25	4.1 ± 5.1	77.8 ± 11.2	1.57 ± 0.26	7.1
Ca II K	3934.78	T2	2.67 ± 0.32	1.0 ± 3.0	51.3 ± 6.9	1.80 ± 0.30	8.4
Ca II H	3969.59	T1	2.56 ± 0.30	−4.4 ± 2.5	43.2 ± 5.8	1.78 ± 0.29	8.5
Ca II H	3969.59	T2	2.76 ± 0.49	−2.1 ± 1.9	21.5 ± 4.4	1.82± 0.45	5.6
Mn I	~4033.91	T1	0.305 ± 0.065	−12.2 ± 1.4	13.9 ± 3.5	1.12 ±0.10	4.7
Mn I	~4033.91	T2	0.271 ± 0.054	−7.4 ± 2.2	23.1 ± 5.3	1.108 ±0.082	5.0
Fe I	~4402.58	T1	0.144 ± 0.031	−4.3 ± 2.2	20.8 ± 5.3	1.059 ± 0.049	4.7
Fe I	~4402.58	T2	0.203 ± 0.030	−8.3 ± 1.6	22.4 ± 3.9	1.082 ± 0.047	6.7
Mg I	4572.38	T1	0.201 ± 0.072	−9.9 ± 2.8	17.4 ± 7.4	1.08 ± 0.11	2.8
Mg I	4572.38	T2	0.213 ± 0.058	−9.4 ± 2.3	15.9 ± 5.6	1.086 ± 0.091	3.7
Mg I b	~5175.97	T1	0.142 ± 0.028	−4.1 ± 2.1	21.4 ± 5.2	1.058 ± 0.045	5.0
Mg I b	~5175.97	T2	0.288 ± 0.038	−7.31 ± 0.71	11.1 ± 1.7	1.115 ± 0.058	7.5
Na I D2	5891.58	T1	0.449 ± 0.049	−5.8 ± 1.0	24.6 ± 3.1	1.174 ± 0.070	9.2
Na I D2	5891.58	T2	0.246 ± 0.037	−5.3 ± 1.4	31.7 ± 5.7	1.099 ± 0.057	6.7
Na I D1	5897.56	T1	0.385 ± 0.051	−5.8 ± 1.0	21.2 ± 3.3	1.148 ± 0.074	7.5
Na I D1	5897.56	T2	0.294 ± 0.042	−5.3 ± 1.4	23.6 ± 4.1	1.117 ± 0.063	7.0
Hα	6564.61	T1	0.48 ± 0.12	−7.48 ± 0.73	5.9 ± 1.8	1.18 ± 0.16	4.0
Hα	6564.61	T2	<0.2	NA	NA	NA	NA
Li I	6709.61	T1	0.173 ± 0.039	−1.8 ± 3.0	26.6 ± 7.6	1.070 ± 0.061	4.4
Li I	6709.61	T2	0.235 ± 0.042	−5.9 ± 1.6	18.7 ± 4.0	1.094 ± 0.064	5.7
K I	7701.09	T1	0.185 ± 0.048	−10.1 ± 2.7	21.9 ± 6.8	1.075 ± 0.076	3.8
K I	7701.09	T2	0.212 ± 0.037	−2.2 ± 2.1	25.5 ± 5.4	1.086 ± 0.057	5.7

Notes. Columns are: line centre in the rest frame (λ), line depth (h), Doppler shift of the line ($V_{\rm wind}$), full width at half maximum (FWHM), and the significance of the detection. All wavelengths are in vacuum. Lines corresponding to the Mg I b T, Mn I, and Fe I have been combined to strengthen the S/N.

Allart et al. 2017). Consequently, we shifted the spectra to the terrestial reference frame before performing any telluric line fitting with `Molecfit`.

In order to perform the telluric line fitting, we selected three telluric regions in the spectra to fit the H_2O and O_2 molecular bands (i.e. 6860–6900 Å, 7160–7340 Å, and 7590–7770 Å). Then, we used the parameters given in Table 2 and ran `Molecfit` to fit the telluric lines (see Fig. 1). We refined the `Molecfit` result until the input and output parameters were the same down to the arithmetic precision achievable using the `Molecfit` graphical user interface. Finally, we gathered the telluric corrected ESPRESSO data and removed the Earth motion using the BERVs already calculated by the ESPRESSO pipeline.

3.2. Transmission spectrum extraction

The telluric line correction has provided us with a set of clean spectra that we can use to extract the planetary signature. Using these corrected ESPRESSO spectra, we extracted the planet signal by means of a procedure based on the technique described by Wyttenbach et al. (2015). Firstly, we shifted the spectra to the stellar reference frame using the radial velocities (RVs) calculated with the ephemeris and Keplerian stellar motion given by Ehrenreich et al. (2020). Secondly, each individual spectrum was flux-scaled by means of a second order polynomial (see Tabernero et al. 2020) to the lowest air-mass spectrum in its corresponding transit observations. The flux level changes from exposure to exposure, due to variations in airmass and atmospheric transparency, and in consequence each individual spectrum must be corrected for these effects. In other words, thanks to this scaling polynomial, the ESPRESSO observations of each transit have been effectively 're-normalized' to the same continuum level.

At this point, we had generated a set of aligned observations (in terms of wavelength and flux) that we used to extract the planetary signature. We organised the observed spectra into two categories: in-transit and out-of-transit, according to the ephemeris given by Ehrenreich et al. (2020). Then, we computed, wavelength by wavelength, the median of the out-of-transit spectra to generate a master stellar spectrum. After this, we divided each individual spectrum by this master spectrum in order to remove the stellar flux from the data. The result of this process is a set of spectra that contain the planetary signal plus the noise left after the removal of the stellar contribution.

After removing the stellar contribution from the data, we found a sinusoidal pattern (wiggles hereafter) on each of the resulting residual spectra. These wiggles are likely caused by an interference pattern induced by the coude train optics. Qualitatively speaking, they have an amplitude of 1% with a period of ~ 30 Å at ~ 6300 Å and might affect the final transmission signature, and in consequence they had to be removed from the transit data. For that reason, we removed them by fitting a set of cubic

splines to the residual spectra using the iSpec code (Blanco-Cuaresma et al. 2014, see Fig. 2). Then, the in-transit residual spectra were shifted in velocity to bring them to the planetary rest frame using the ephemeris given by Ehrenreich et al. (2020). These shifted residual spectra were later merged, wavelength by wavelength, into a single median transmission spectrum. This procedure was applied independently to T1 and T2 to produce two independent transmission spectra for WASP-76b.

4. Stellar characterisation

4.1. Stellar atmospheric parameters

The stellar atmospheric parameters of WASP-76, namely effective temperature ($T_{\rm eff}$), surface gravity ($\log g$), microturbulence (ξ), and metallicity ([Fe/H]), were calculated using the equivalent width (EW) method by means of the StePar[5] code (Tabernero et al. 2019). The atmospheric parameters were computed using the master spectrum from Sect. 3.2. The latest state-of-the-art version of StePar relies on the 2017 version of the MOOG code (via the abfind driver, see Sneden 1973) and a grid of MARCS stellar atmospheric models (Gustafsson et al. 2008). We employed the selection of Fe I and Fe II following the line list given by Tabernero et al. (2019) for metal-rich dwarf stars. The available atomic data of these iron lines were taken from the public version of the *Gaia*-ESO line list (Heiter et al. 2015). As a damping prescription, we used the Anstee-Barcklem-O'Mara (ABO, see Barklem et al. 1998) data (if available), through option 1 of MOOG. In addition, we used ARES[6] (Sousa et al. 2015) to measure the EWs of the Fe I,II lines used.

We only considered measured lines with 10 mÅ < EW < 120 mÅ to avoid problems with line profiles of very intense lines and tentatively incorrect EW measurements of extremely weak lines. The atmospheric parameters can then be inferred from the previously measured Fe I–Fe II line list. The minimisation procedure of StePar is the downhill simplex algorithm (Press et al. 2002), which tries to minimise a quadratic form composed of the excitation and ionisation equilibrium conditions to find the best parameters of the target star. StePar iterates until $\log \epsilon$(Fe I) and $\log \epsilon$(Fe II) stand for the Fe abundance returned by the Fe I and Fe II lines, respectively, and $\log$(EW/λ) is their reduced equivalent width. StePar iterates until the slopes of χ vs. $\log \epsilon$(Fe I) and $\log$(EW/λ) vs. $\log \epsilon$(Fe I) are virtually zero, meaning excitation equilibrium is reached, and it imposes ionisation equilibrium, so that $\log \epsilon$(Fe I) = $\log \epsilon$(Fe II). The stellar parameters derived for WASP-76 in this work can be found in Table 3.

We also calculated stellar atmospheric parameters using the ARES+MOOG code (Sousa et al. 2008, 2018; Santos et al. 2013) and obtained similar results to those provided by StePar: $T_{\rm eff}$ = 6329 ± 24 K, $\log g$ = 4.20 ± 0.03 dex, ξ = 1.54 ± 0.03 km s^{-1}, and [Fe/H]=0.37 ± 0.02 dex. Both ARES+MOOG and StePar are similar implementations of the EW method. ARES+MOOG employs a similar workflow to that of StePar, however it implements KURUCZ stellar atmospheric models (Kurucz 1993), a solar calibrated $\log gf$ Fe I,II line list (Sousa et al. 2008), and the damping option 0 of MOOG. In addition, West et al. (2016) calculated the following stellar parameters of $T_{\rm eff}$ = 6250 ± 100 K, $\log g$ = 4.13 ± 0.02 dex, ξ = 1.4 ± 0.1 km s^{-1}, and [Fe/H] = 0.23 ± 0.1 dex. These values

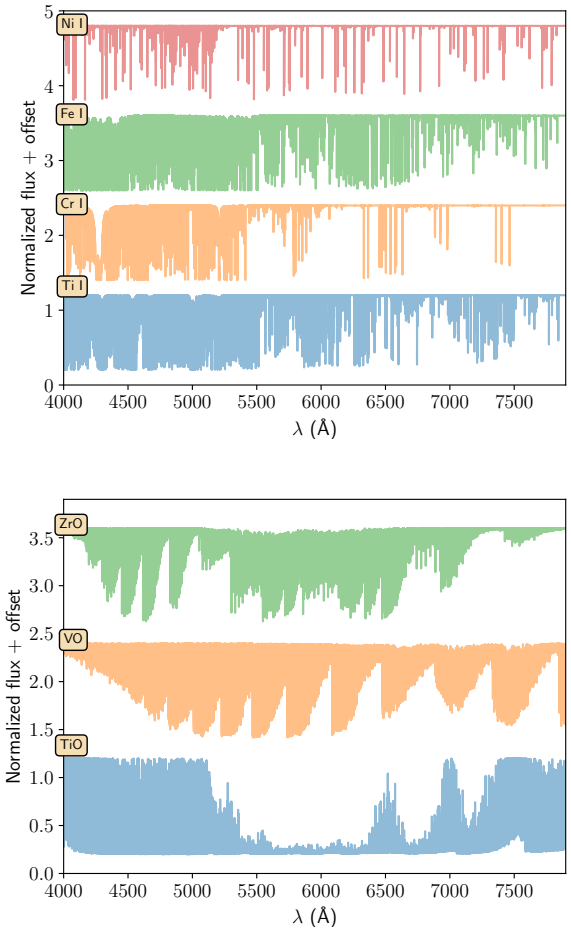

Fig. 4. Synthetic models generated with turbospectrum for the different atomic and molecular species. All of them have been degraded to R = 140 000.

are in good agreement with those calculated with StePar and ARES+MOOG codes.

4.2. Stellar mass and radius

We used the PARAM web interface[7] (da Silva et al. 2006) to calculate the mass (M_*) and radius (R_*) of WASP-76. We used the stellar parameters calculated with StePar along with the *Gaia* DR2 Parallax (Gaia Collaboration 2018), the visual magnitude (m_V) given by West et al. (2016), and the PARSEC stellar evolutionary tracks and isochrones (Bressan et al. 2012) to obtain a mass of 1.45 ± 0.02 $M_\odot$ and a radius of 1.77 ± 0.07 $R_\odot$. Our values are consistent with those provided by Ehrenreich et al. (2020), who reported M_* = 1.46 ± 0.02 $M_\odot$ and R_* = 1.76 ± 0.07 $R_\odot$. On the other hand, West et al. (2016) obtained 1.46 ± 0.07 $M_\odot$ and 1.73 ± 0.04 $R_\odot$, which are both consistent with the values derived in this work.

4.3. Chemical abundances

We calculated the chemical abundances of WASP-76 (see Table 4) by means of the EW method for the following atomic species: Li I C I, O I, Na I, Mg I, Si I, Ca I, Ti I, Cr I, Mn I, and Ni I. Moreover, the atomic data for each atomic species under analysis were collected from the *Gaia*-ESO (GES) line list

[5] https://github.com/hmtabernero/StePar
[6] https://github.com/sousasag/ARES
[7] http://stev.oapd.inaf.it/cgi-bin/param_1.3

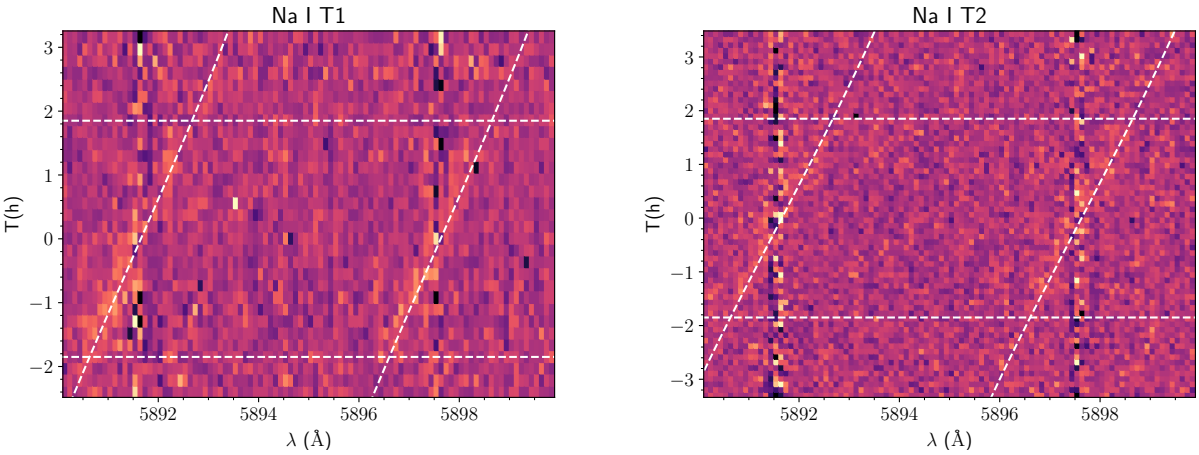

Fig. 5. Na Double tomography for transit 1 (*left*) and transit 2 (*right*). Time 0.0 h corresponds to the mid-transit according to the planetary ephemeris given in Table 3. Each tile represents a 0.1 Å bin. These plots are qualitative and have been generated only for visualisation purposes.

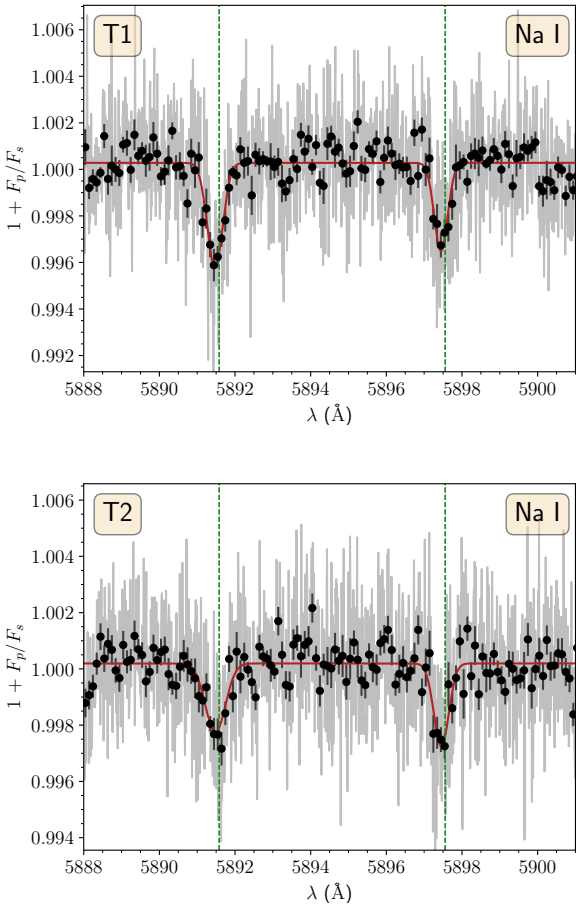

Fig. 6. Transmission spectra around the Na I doublet: *top* (T1), *bottom* (T2). The grey line represents the original transmission spectrum of WASP-76b, whereas the black dots represent a binning of 0.1 Å. The red line represents the best fit to the data. The rest-frame wavelength of each individual line is represented by a dashed green vertical line.

(Heiter et al. 2015). We measured an $EW = 29.2$ mÅ for the Li I line at 6709.61 Å by means of a Gaussian fit performed using the Levenberg–Marquardt algorithm (LMA) implemented in the python library `SciPy` (Virtanen et al. 2020). The EWs of the other elements were measured by means of the ARES code. Then, we interpolated a model atmosphere from the MARCS

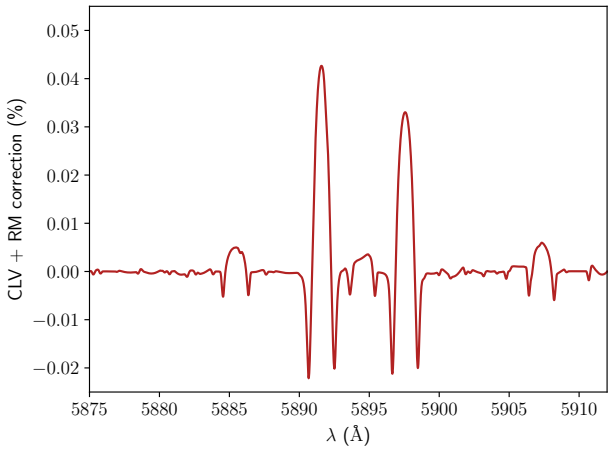

Fig. 7. Center to limb variation (CLV) and Rossiter-McLaughlin (RM) correction around the Na I lines.

stellar atmospheric grid (Gustafsson et al. 2008) and we used the MOOG code (Sneden 1973) to derive the abundances for WASP-76. The O I abundance was later corrected for NLTE effects thanks to the corrections given by Sitnova et al. (2013)[8]. Then, we used C I and O I to derive a carbon-to-oxygen ratio (C/O) of 0.51 ± 0.03, which in turn is consistent with the solar value. Finally, the atomic parameters employed to calculate the abundances can be found in Table A.1.

5. Transmission spectrum analysis

The procedure employed in this work delivers the entire ESPRESSO spectrum of WASP-76b simultaneously. This is possible via the stable and consistent wavelength calibration of the ESPRESSO data. The extracted transmission spectra for T1 and T2 are depicted in Fig. 3. Using these two spectra, we can identify tentative spectral features by visual inspection and perform a cross-correlation using a binary mask built for a given atomic or molecular species. We explored the presence of the following atomic species by direct inspection of the transmission spectrum: H I, Li I, Na I, Mg I, Ca II, Mn I, Fe I, and K I. In addition, we explored the presence of other species via a cross-correlation

[8] Using the web interface at `http://nlte.mpia.de`

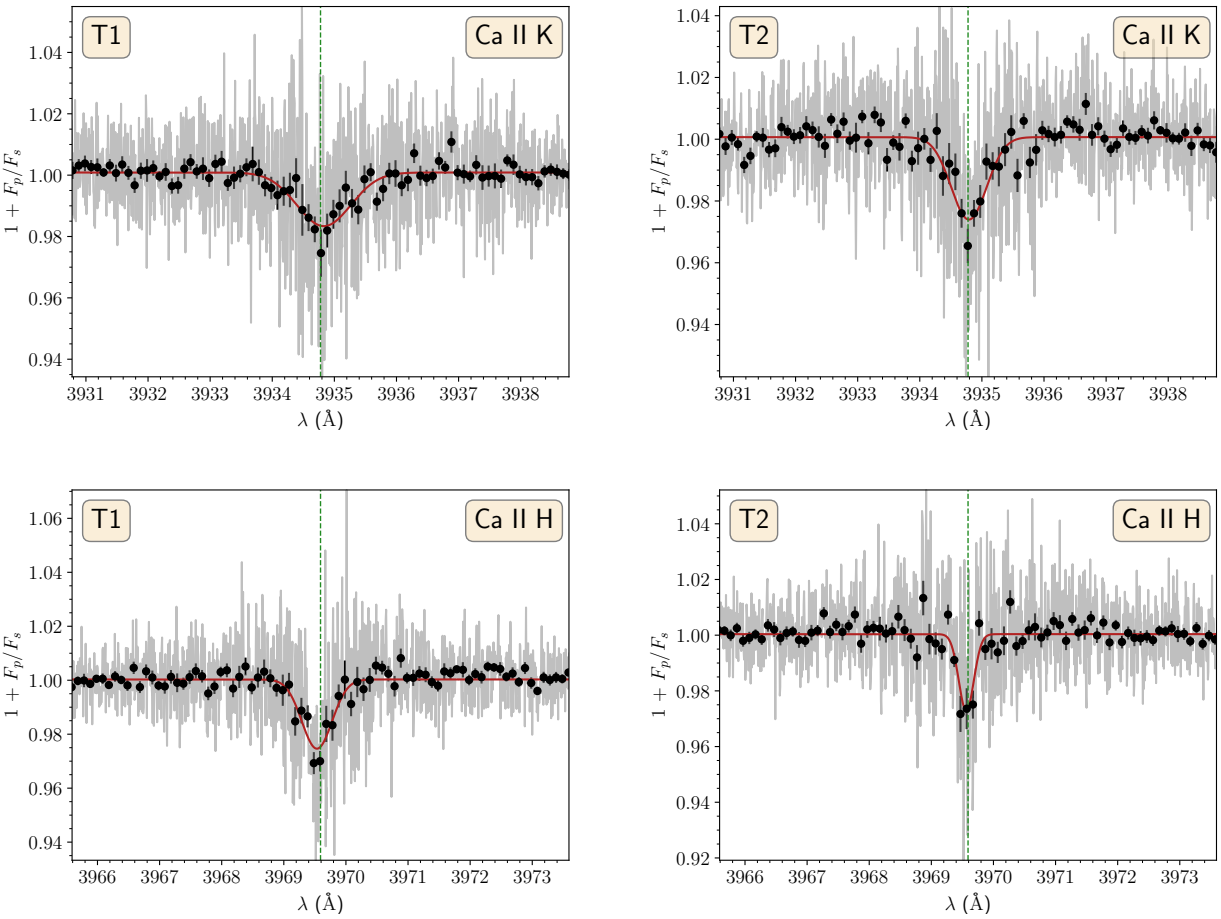

Fig. 8. Same as Fig. 6 but for ii H and K lines.

function (CCF) analysis: Ti I, Cr I, Fe I, and Ni I in addition to the diatomic molecules TiO, VO, and ZrO.

Each tentative atomic feature directly seen in the transmission spectrum of WASP-76b has to be scrutinised for its significance. Thus, we modelled each individual feature with a Gaussian profile plus the continuum level. The model fitting is then performed by means of the LMA implemented in the python library `SciPy` (Virtanen et al. 2020). The LMA explores the parameter space that provides us with valuable information about each spectroscopy feature in consideration. In summary, our modelling provides the Gaussian parameters of the line under analysis (i.e. centre, amplitude, depth, and width) alongside their uncertainties. We also calculated the Doppler shift ($V_{\rm wind}$) of each line to explore any tentative planetary winds (see, e.g. Hoeijmakers et al. 2018; Casasayas-Barris et al. 2019). Moreover, we derived effective planetary radii at the centre of each feature (R_λ) in units of the radius of the planet ($R_{\rm p}$) at the centre of each individual atomic feature. Thus, we used the following expression: $R_\lambda = \sqrt{1 + h/\delta}\ R_{\rm p}$, where h is the line depth of a given absorption feature in the transmission spectrum, and δ is the transit depth of the planet. All these results can be found in Table 5. Regarding these lines, we produced a series of tomography plots (see Figs. 5, and A.2–A.5) in order to explore the passage of the planet with time for each transit, which allows us to confirm the presence of the planetary signal. However, some lines are perhaps too weak to be directly seen in the tomography plots.

In addition, the detection of some atomic or molecular species in the atmosphere of the planet can be achieved by cross-correlating the planetary signal with a synthetic spectrum. To that particular aim, we calculated an atmospheric structure of WASP-76b by means of the HELIOS code[9] (Malik et al. 2017, 2019). In order to generate a model spectrum, we need a radiative transfer code to input the planet atmospheric structure calculated by HELIOS. The aforementioned atmospheric structure consists of a set of atmospheric layers containing the gaseous pressure ($P_{\rm g}$), temperature (T), and geometrical depth. These quantities are necessary to solve the radiative transfer equation in order to produce a synthetic model spectrum. We employed `turbospectrum`[10] to solve the radiative transfer problem (Plez 2012) alongside seven different line lists comprised of the following atomic and molecular species: Cr I, Ti I, Fe I, Ni I, TiO, VO, and ZrO. The atomic data were downloaded using the VALD3 interface[11] (Ryabchikova et al. 2015), while the molecular data for TiO, VO, and ZrO were gathered from Plez (1998, 2003), and McKemmish et al. (2016), respectively. Furthermore, `turbospectrum` is a general purpose radiative transfer tool that can generate high-resolution synthetic spectra by solving the problem of radiative transfer in spherical geometry. The resulting synthetic spectra (see Fig. 4) were later converted into binary line masks that we used to perform a cross-correlation against our two transmission spectra. To perform the cross-correlation, we employed the `iSpec` (Blanco-Cuaresma et al. 2014) code, which in turn implements the algorithm described in

[9] https://github.com/exoclime/HELIOS
[10] https://github.com/bertrandplez/Turbospectrum2019
[11] http://vald.astro.uu.se/

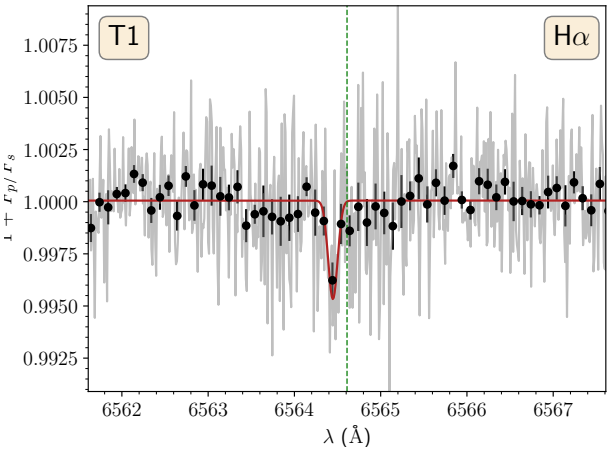

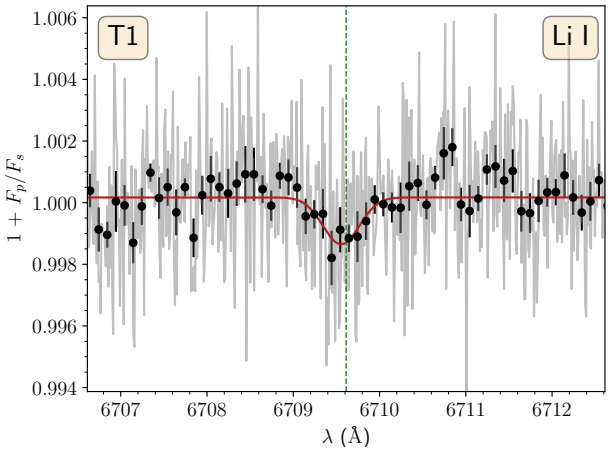

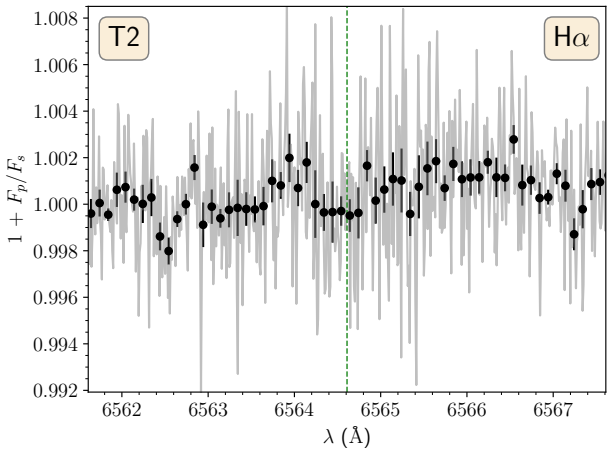

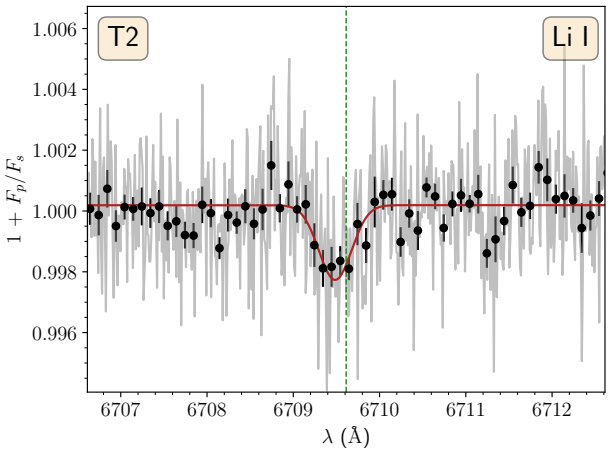

Fig. 9. Same as Fig. 6 but for the Hα line.

Fig. 10. Same as Fig. 6 but for the Li I line.

Pepe et al. (2002) to calculate the CCF. The goal of the cross-correlation technique is to combine thousands of spectral features to produce an imprint that we will be able detect.

5.1. Na I

Firstly, we verified that our procedure was extracting the signals for lines already reported in the literature, such as the Na I doublet. The detection of the Na I Doublet in WASP-76b has already been reported by Seidel et al. (2019) and Edwards et al. (2020). We clearly detected both lines in the 2D-map moving with the planet velocity (see Fig. 5). Our final spectrum of the Na I doublet is shown in Fig. 6. Our detection is 9.2 and 7.5 σ levels for T1, and 6.5 and 7 σ for T2. These detections are more significant than those obtained by Seidel et al. (2019) using HARPS data. In addition, we verified the effect of the Rossiter-McLaughlin effect on our extraction by means of the modelling described in Casasayas-Barris et al. (2019) using the ephemeris given by Ehrenreich et al. (2020). We find that the effect is not significant (0.04%) given our error bars for the two transits of WASP-76 b (see Fig. 7).

5.2. Ca II

The Ca II H (3969.59 Å) and Ca II K (3934.78 Å) lines are visible in the transmission spectrum (see Fig. 8), our Gaussian fits shows that they are significant at the level of 8.5–7.1 σ for T1 and 5.6–8.4 σ for T2. These two lines are the most prominent features of the transmission spectrum of WASP-76, being one order of magnitude deeper than the other atomic features (~2–3%). In fact, they might be originated by photo-ionisation in the upper part of the highly irradiated planetary exosphere (Yan et al. 2019). Moreover, their intrinsic depth points towards a high formation altitude (see Table 5) as our calculated R_λ is 1.78–1.57 R_p (T1) and 1.82–1.80 R_p (T2).

5.3. Balmer lines

The H_α line at 6564.61 Å is present in T1, whereas T2 shows a little bump rather than a proper line (see Fig. 9). Thus, it is not possible to confirm the presence of atomic hydrogen in the atmosphere using only T2, and for T1 we find a depth at 0.48 ± 0.12%. We also explored other Balmer lines (Hβ, Hγ), but none of them are visible in the planetary transmission spectrum. The T2 data have a higher quality than T1, which in turn implies that if Hα absorption were present in T2 with the same intensity as in T1, we should have detected it. Interestingly enough, no study to the present date has provided an upper limit to the presence of Hα in the spectrum of WASP-76b. von Essen et al. (2020) explored the transmission of spectrum of WASP-76b using HST optical spectra and did not find any evidence of strong absorption due to Hα. In contrast, our findings at a higher resolution might be evidence for Hα variability from the planetary atmosphere, given that the line is not seen in T2. However, the available data are not sufficient to confirm this scenario.

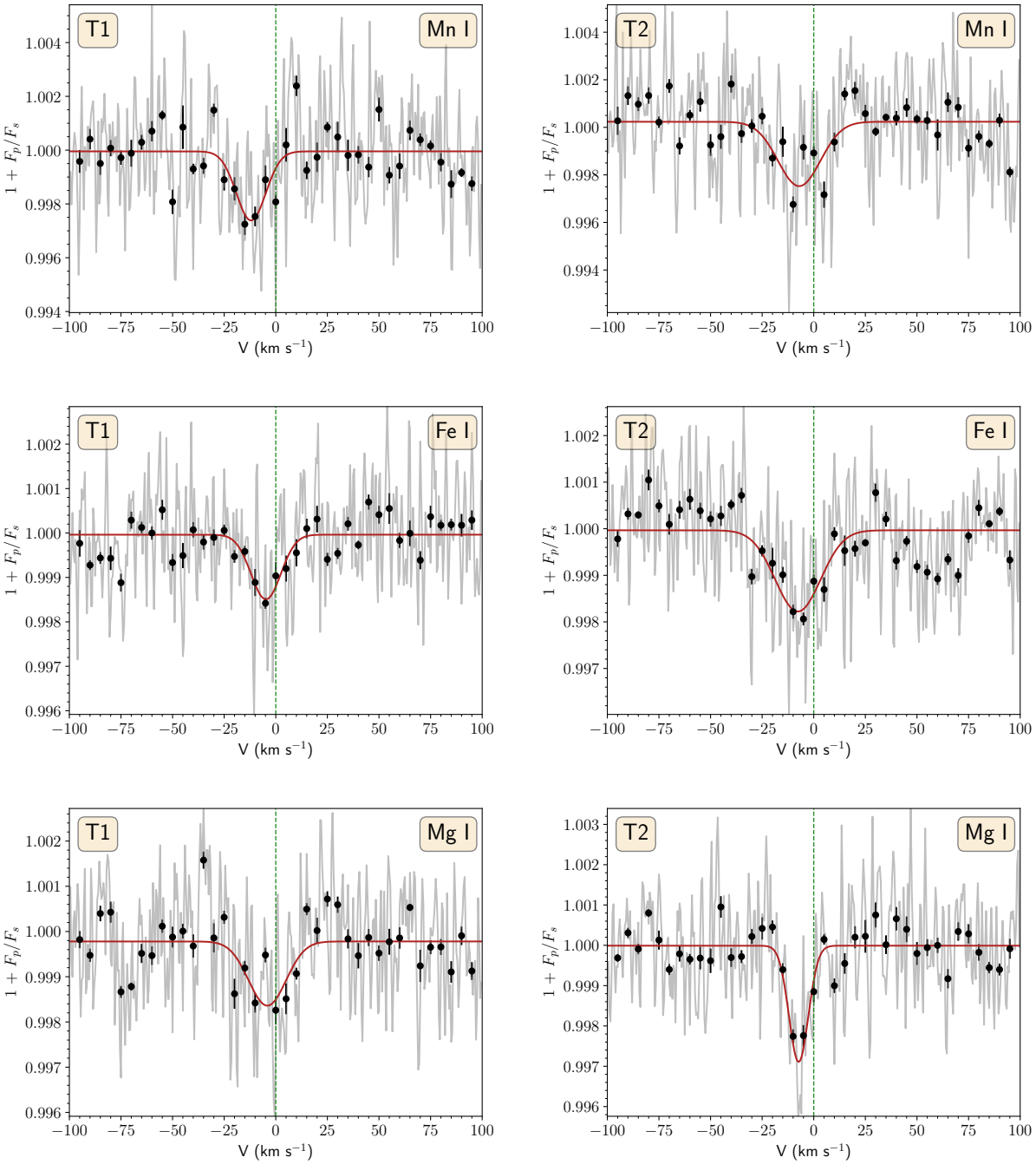

Fig. 11. Same as Fig. 6 but for other elements. Here, we represent the combination of several lines in velocity space to strengthen the signal. Black points represent a binning of 10 km s^{-1} and the green dashed line represents the 0 km s^{-1} mark.

5.4. Li I

The planet WASP-76b is expected to have Li in its atmosphere because sub-stellar objects with masses below ≈55 $M_{\rm Jup}$ do not deplete this element at any moment during their evolution (Chabrier et al. 2000; Baraffe et al. 2015). Consequently, WASP-76b should maintain the amount of lithium in its atmosphere that was present in the protoplanetary disc from which it was supposedly formed. In fact, the presence of Li was modelled by Chen et al. (2018) for another giant planet. The Li I absorption feature at 6709.61 Å is detected in the ESPRESSO spectra of the planet WASP-76b (see Fig. 10). We found that Li I is moving with the planet velocity in T2, whereas we find a small trace during T1 (see Fig. A.5). The Li I line is more significant for T2 than T1 (5.7σ vs. 4.4σ) and it can be easily explained by the cadence of the observations of T2 in contrast with T1. To the best of our knowledge, this is the first reported detection of Lithium using high-resolution spectroscopy (in Borsa et al. 2021, there is also a report on the detection of lithium in another giant planet using ESPRESSO data).

5.5. Fe I

Interestingly enough, the accuracy of the ESPRESSO data has allowed us to detect actual Fe I lines in the transmission spectra of WASP-76 b. In particular, our two transit spectra show a few tentative neutral iron lines in the range of ≈4377–4430 Å. The

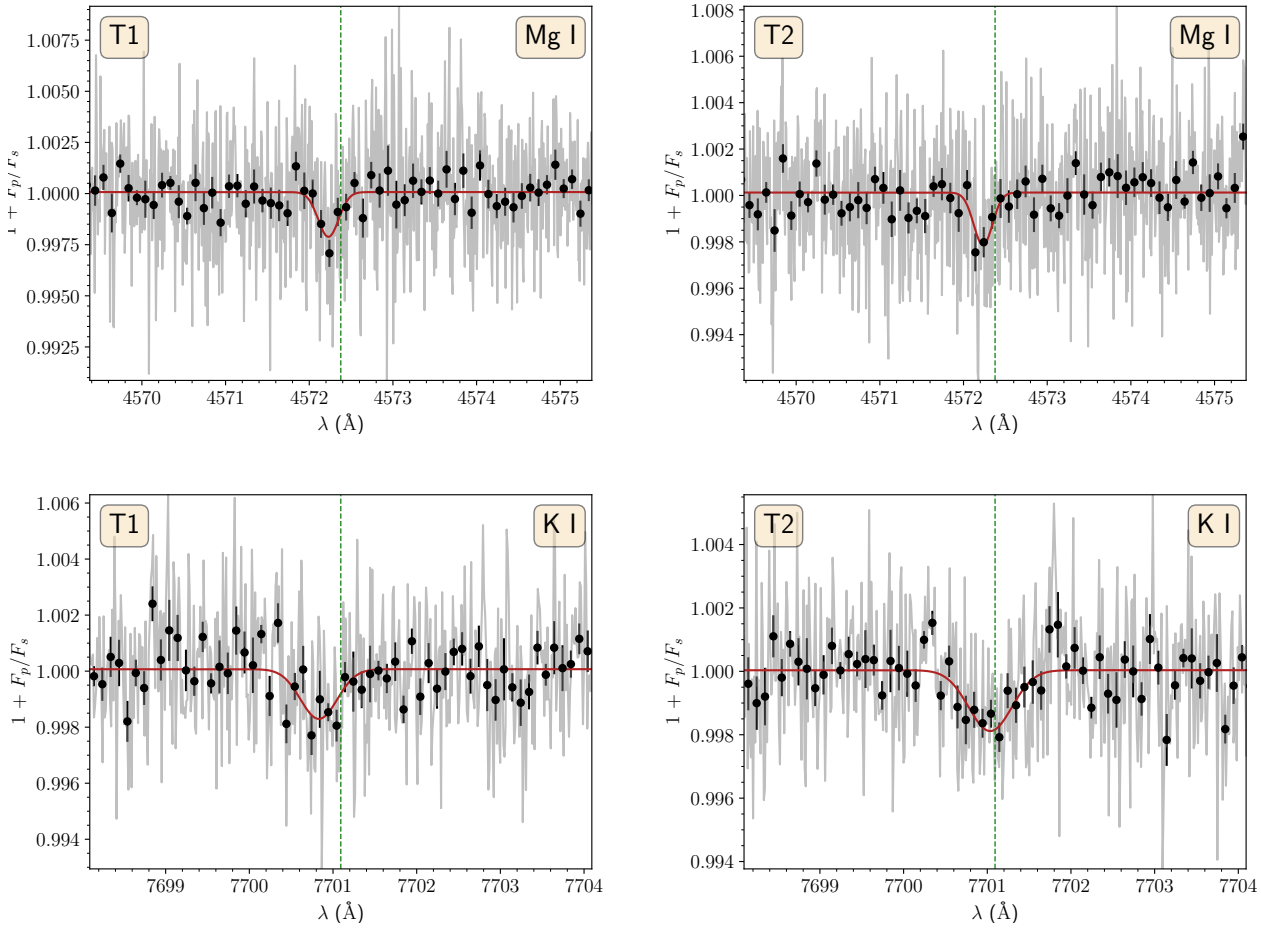

Fig. 12. Same as Fig. 11 but for Mg I and K I.

following lines are seen in the spectrum of WASP-76b: 4377.16, 4384.78, 4406.26, 4416.17, and 4428.55 Å. To increase the S/N of the profile of the Fe lines, we merged all of them into a single line in velocity space (see Fig. 11). The combination of these lines is stronger for T2 (6.7σ) than for T1 (4.7 σ). The detection of these lines is in agreement with the results of the CCF against an Fe I binary mask (see Fig. 13). In this work, we found a depth of 255 ± 20 ppm (T1) and 182 ± 12 ppm (T2). These two values correspond to central velocities of −8.27 ± 0.25 km s^{-1} and −8.76 ± 0.56 km s$^{-1,}$ respectively, and to a detection at 12.8 σ and the 18.2 σ levels for T1 and T2, respectively (see Table 6). Overall, our results reinforce those presented by Ehrenreich et al. (2020) for WASP-76b.

5.6. Mg I, K I, and Mn I

The Mg I line at 4572.38 Å seems to be in the transmission spectrum with a significance of ∼2.8 σ for T1 and 3.7 σ for T2 (see Fig. 12). In addition to this Mg I, we find that the space-velocity combined magnesium triplet lines (5168.76, 5174.13, and 5185.05 Å) are clearly seen at the 7.5 σ level for T2 (see Fig. 11). Regarding K I, the transmission maps show a small imprint leaving a partial trace that we can barely see in our maps (see Fig. A.3). However, the line is present at the 5.7 σ level in T2. We also report the detection of the Mn I triplet lines at 4031.89, 4034.20, and 4035.62 Å. Again, we combined these three lines in velocity space and we find that their significance is in the range of 4.7-5.0 σ.

Table 6. Cross-correlation data for analysed atomic and molecular species.

Element	Transit	Depth (ppm)	$V_{\rm wind}$ (km s^{-1})	$FWHM$ (km s^{-1})
Ti I	T1	<61	NA	NA
Ti I	T2	<60	NA	NA
Cr I	T1	<77	NA	NA
Cr I	T2	<78	NA	NA
Fe I	T1	255 ± 20	−8.27 ± 0.25	6.62 ± 0.59
Fe I	T2	182 ± 12	−8.75 ± 0.56	18.0 ± 1.3
Ni I	T1	<130	NA	NA
Ni I	T2	<122	NA	NA
TiO	T1	<6	NA	NA
TiO	T2	<6	NA	NA
VO	T1	<9	NA	NA
VO	T2	<8	NA	NA
ZrO	T1	<9	NA	NA
ZrO	T2	<8	NA	NA

5.7. Ti I, Cr I, and Ni I

We also explored the presence of Ti I, Cr I, and Ni I in our data using a cross-correlation method. For the most part, our

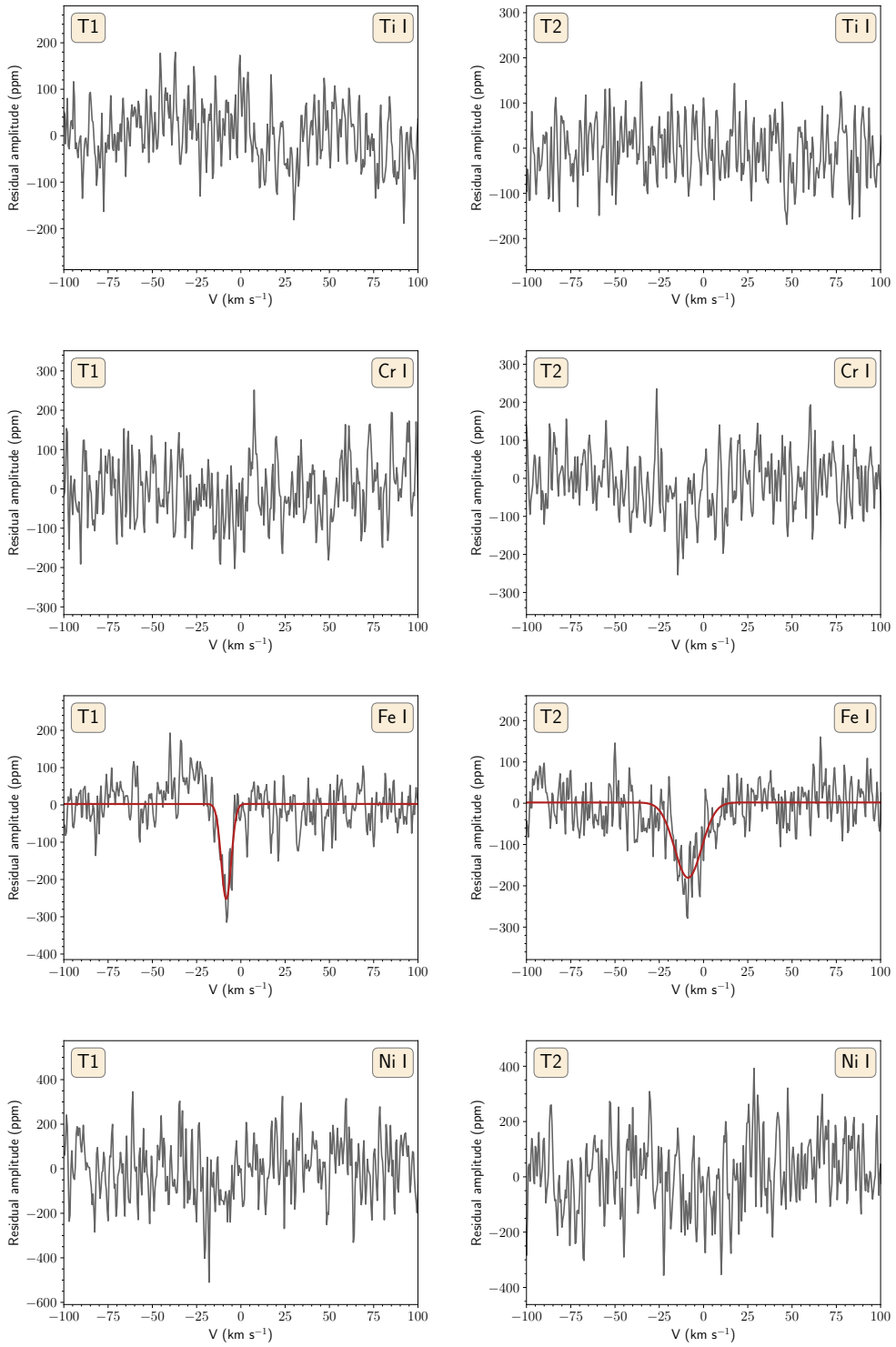

Fig. 13. Cross-correlation function against our line masks for Ti I, Cr I, Fe I, and Ni I. The black line represents CCF, whereas the red line represents the best fit to the Fe I CCF.

search was unsuccessful and we could only calculate upper limits to their presence of ∼60 ppm (Ti I), ∼77 ppm (Cr I), and ∼130 ppm (Ni I). Finally, the data regarding these elements and their respective CCFs can be found in Table 6 and in Fig. 13.

5.8. Diatomic molecules: TiO, VO, and ZrO

These three diatomic molecules are important absorbers in cool stellar atmospheres with a non-negligible opacity source as already shown by Van Eck et al. (2017). The CCFs calculated in this work do not show any trace of them in our data, as shown in Fig. A.1. However, we can place a conservative upper limit on their presence of ≤10 ppm (see Table 6). Interestingly, the TiO atomic data were recently improved by the exomol team (see McKemmish et al. 2019). As a result, we generated a new TiO model spectrum using the exomol line list (McKemmish et al. 2019) and performed a CCF against it. We found an upper limit to the presence of TiO of 6 ppm, which in turn is in agreement with

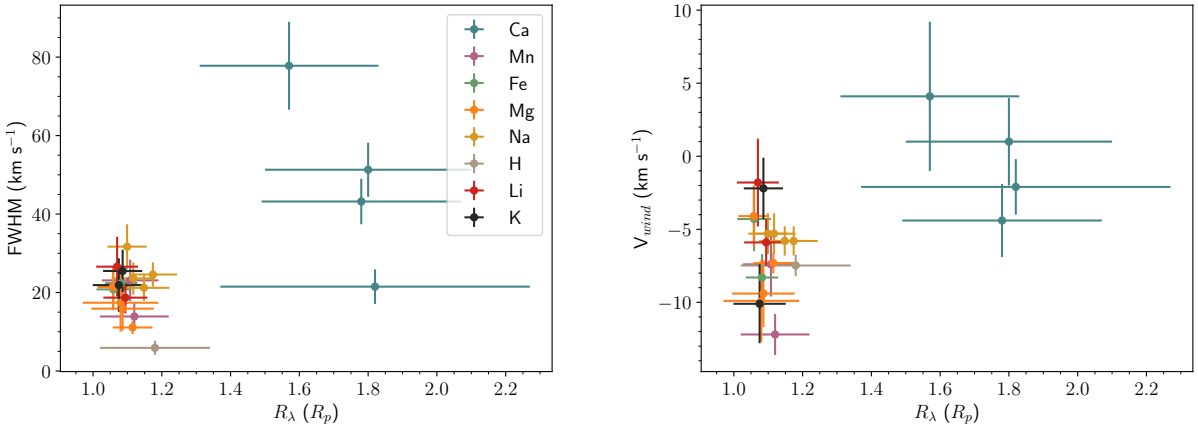

Fig. 14. FWHM and $V_{\rm wind}$ for the lines studied in this work vs. R_λ.

what we obtained with the Plez (1998) line list (see Table 6). In all, these state-of-the-art line lists might be not accurate enough to confidently retrieve the presence of TiO in the atmosphere of WASP-76b. Despite this, we can think of two scenarios for this particular planet: these features are either really weak or they are hidden due to other effects. However, clouds might be responsible for the weakening of the molecular bands and in the planetary spectrum (Charnay et al. 2015). In addition, another explanation might stem from the transport of molecules to the night side of the planet (Nugroho et al. 2017). In all, TiO and VO should dominate the spectrum in the optical wavelength range (Van Eck et al. 2017), given the equilibrium temperature of the planet. Other studies have explored the atmosphere of WASP-76b using HST data (Edwards et al. 2020; von Essen et al. 2020) and modelled the atmosphere of the planet. In fact, the transmission spectrum and the modelling of von Essen et al. (2020) did not present any evidence for TiO absorption in the optical wavelength range. This is consistent with our non-detections using ESPRESSO data. Interestingly, the nearly solar C/O calculated here for WASP-76 does not suggest that the atmosphere of the WASP-76b is driven by a carbon-rich chemistry. However, clouds might be responsible for the weakening of the molecular bands and in the planetary spectrum (Charnay et al. 2015). In addition, another explanation might stem from the transport of molecules to the night side of the planet (Nugroho et al. 2017).

6. Summary and conclusions

We analysed two transits of the UHJ WASP-76b using ESPRESSO at the VLT. In this work, we generated two independent transmission spectra covering the available wavelength range. Using these spectra, we have been able to detect features that were not reported in previous studies: Li I, Mg I, K I, Ca II, and Mn I. In addition, our work strengthens the previous detections of Na I (Seidel et al. 2019; von Essen et al. 2020) and Fe I (Ehrenreich et al. 2020).

We find that most lines are blueshifted with respect to their rest-frame wavelengths (see Fig. 14). The median is -5.6 ± 4.2 km s^{-1} for T1, and -5.2 ± 3.1 km s^{-1} for T2. These shifts are probably due to planetary winds and are frequently reported in the literature (see, e.g. Casasayas-Barris et al. 2019; Hoeijmakers et al. 2019; Gibson et al. 2020; Ehrenreich et al. 2020).

Interestingly, our calculations indicate that the Ca II lines are formed in higher layers than the other lines ($\sim$1.6−1.8 $R_{\rm p}$, see Table 5), which points towards an extended exosphere. This has already been reported for other planets such as MASCARA-2b (Casasayas-Barris et al. 2019), WASP-33b (Yan et al. 2019), and WASP-121b (Borsa et al. 2021). In addition, their intrinsic widths are in all instances higher than $\sim$20 km s^{-1} (see Fig. 14). In addition, the Hα line seen in T1 is much narrower compared to the other atomic features. Its width is $\sim$6 km s^{-1}, which is greater than the resolving power of our data ($R = 140\,000$; $FWHM = 2.1$ km s^{-1}). In all, the measured FWHM for this line is in principle physically possible, and its absence in T2 might be indicative of atmospheric variability. However, the current data are not sufficient to fully explore this scenario.

In addition, our data show that the K I absorption line is weaker than the Li I feature, a fact that is unexpected for a near-solar composition where K is much more abundant than Li (both atoms have very similar electronic structures). The observations suggest that Li is at least as abundant as K in the investigated planetary atmospheric layers. This requires scenarios that have not been explored in exoplanetary atmospheres so far; for example, lithium production in situ or a strongly inhomogeneous distribution of the chemical abundances within the atmosphere.

Regarding the molecular species in WASP-76b, we could not find any signs of TiO, VO, or ZrO. They are either not present in the atmosphere of WASP-76b or their intensity is well below the minimum noise level in these observations. Finally, we demonstrate that we are able to reduce the noise of the exoplanetary data using ESPRESSO to the extent that we can detect many planetary atomic features by means of a single transmission spectrum.

Acknowledgements. This work was supported by FCT – Fundação para a Ciência e a Tecnologia through national funds and by FEDER through COMPETE2020 – Programa Operacional Competitividade e Internacionalização by these grants: UID/FIS/04434/2019; UIDB/04434/2020; UIDP/04434/2020; PTDC/FIS-AST/32113/2017 & POCI-01-0145-FEDER-032113; PTDC/FIS-AST/28953/2017 & POCI-01-0145-FEDER-028953; PTDC/FIS-AST/28987/2017 & POCI-01-0145-FEDER-028987. V.A., S.G.S., S.C.C.B. acknowledge support from FCT through Investigador FCT contracts ns° IF/00650/2015/CP1273/CT0001; IF/00028/2014/CP1215/CT0002; IF/01312/2014/CP1215/CT0004. S.G.S acknowledges the support from FCT through Investigador FCT contract nr. CEECIND/00826/2018 and POPH/FSE (EC). J.P.F., O.D., and J.H.C.M. acknowledge support from FCT through national funds in the form of a work contract with the references DL 57/2016/CP1364/CT0005; DL 57/2016/CP1364/CT0004; DL 57/2016/CP1364/CT0007. H.M.T. and M.R.Z.O. acknowledge financial support from the Spanish Ministerio de Ciencia, Innovación y Universidades (MICIU) through project AYA2016-79425-C3-2. A.S.M., R.R., J.I.G.H., C.A.P. acknowledge financial support from the Spanish MICIU project AYA2017-86389-P. J.I.G.H. acknowledges financial support from the Spanish MICIU under the 2013 Ramón y Cajal program RYC-2013-14875. This work has been carried out within the framework of the National Centre

of Competence in Research PlanetS supported by the Swiss National Science Foundation. The authors acknowledge the financial support of the SNSF. The INAF authors acknowledge financial support of the Italian Ministry of Education, University, and Research with PRIN 201278X4FL and the "Progetti Premiali" funding scheme. This project has received funding from the European Research Council (ERC) under the European Union's Horizon 2020 research and innovation programme (project FOUR ACES; grant agreement No 724427). N.J.N. acknowledges support from FCT through Investigador FCT contract and exploratory project IF/00852/2015, and project PTDC/FIS-OUT/29048/2017. J.V.S. acknowledges funding from the European Research Council (ERC) under the European Union's Horizon 2020 research and innovation programme (project Four Aces; grant agreement No. 724427).

References

Alam, S., Albareti, F. D., Allende Prieto, C., et al. 2015, ApJS, 219, 12
Allart, R., Lovis, C., Pino, L., et al. 2017, A&A, 606, A144
Allart, R., Bourrier, V., Lovis, C., et al. 2018, Science, 362, 1384
Allart, R., Bourrier, V., Lovis, C., et al. 2019, A&A, 623, A58
Alonso-Floriano, F. J., Snellen, I. A. G., Czesla, S., et al. 2019, A&A, 629, A110
Baraffe, I., Homeier, D., Allard, F., & Chabrier, G. 2015, A&A, 577, A42
Barklem, P. S., Anstee, S. D., & O'Mara, B. J. 1998, PASA, 15, 336
Barman, T. S., Konopacky, Q. M., Macintosh, B., & Marois, C. 2015, ApJ, 804, 61
Blanco-Cuaresma, S., Soubiran, C., Heiter, U., & Jofré, P. 2014, A&A, 569, A111
Borsa, F., Allart, R., Casasayas-Barris, N., et al. 2021, A&A, 645, A24
Borucki, W. J., Koch, D., Basri, G., et al. 2010, Science, 327, 977
Bressan, A., Marigo, P., Girardi, L., et al. 2012, MNRAS, 427, 127
Casasayas-Barris, N., Pallé, E., Yan, F., et al. 2019, A&A, 628, A9
Casasayas-Barris, N., Pallé, E., Yan, F., et al. 2020, A&A, 635, A206
Casasayas-Barris, N., Pallé, E., Stranget, M., et al. 2021, A&A, in press, https://doi.org/10.1051/0004-6361/202039539
Chabrier, G., Baraffe, I., Allard, F., & Hauschildt, P. 2000, ApJ, 542, 464
Charbonneau, D., Brown, T. M., Noyes, R. W., & Gilliland, R. L. 2002, ApJ, 568, 377
Charnay, B., Meadows, V., & Leconte, J. 2015, ApJ, 813, 15
Chen, G., Pallé, E., Welbanks, L., et al. 2018, A&A, 616, A145
Cosentino, R., Lovis, C., Pepe, F., et al. 2012, SPIE Conf. Ser., 8446, 84461V
da Silva, L., Girardi, L., Pasquini, L., et al. 2006, A&A, 458, 609
Edwards, B., Changeat, Q., Baeyens, R., et al. 2020, AJ, 160, 8
Ehrenreich, D., Lovis, C., Allart, R., et al. 2020, Nature, 580, 597
Gaia Collaboration (Brown, A. G. A., et al.) 2018, A&A, 616, A1
Gardner, J. P., Mather, J. C., Clampin, M., et al. 2006, Space Sci. Rev., 123, 485
Gibson, N. P., Merritt, S., Nugroho, S. K., et al. 2020, MNRAS, 493, 2215
Gustafsson, B., Edvardsson, B., Eriksson, K., et al. 2008, A&A, 486, 951
Heiter, U., Lind, K., Asplund, M., et al. 2015, Phys. Scr., 90, 054010
Hoeijmakers, H. J., Ehrenreich, D., Heng, K., et al. 2018, Nature, 560, 453
Hoeijmakers, H. J., Ehrenreich, D., Kitzmann, D., et al. 2019, A&A, 627, A165
Hoeijmakers, H. J., Seidel, J. V., Pino, L., et al. 2020, A&A, 641, A123
Kausch, W., Noll, S., Smette, A., et al. 2015, A&A, 576, A78
Kurucz, R. 1993, ATLAS9 Stellar Atmosphere Programs and 2 km/s grid. Kurucz CD-ROM No. 13. Cambridge, 13
Mahadevan, S., Ramsey, L. W., Terrien, R., et al. 2014, SPIE, 543, 552
Malik, M., Grosheintz, L., Mendonça, J. M., et al. 2017, AJ, 153, 56
Malik, M., Kitzmann, D., Mendonça, J. M., et al. 2019, AJ, 157, 170
Mayor, M., Pepe, F., Queloz, D., et al. 2003, The Messenger, 114, 20
McKemmish, L. K., Yurchenko, S. N., & Tennyson, J. 2016, MNRAS, 463, 771
McKemmish, L. K., Masseron, T., Hoeijmakers, H. J., et al. 2019, MNRAS, 488, 2836
Moutou, C., Boisse, I., Hébrard, G., et al. 2015, SF2A-2015: Proceedings of the Annual meeting of the French Society of Astronomy and Astrophysics, 205
Nortmann, L., Pallé, E., Salz, M., et al. 2018, Science, 362, 1388
Nugroho, S. K., Kawahara, H., Masuda, K., et al. 2017, AJ, 154, 221
Parmentier, V., Line, M. R., Bean, J. L., et al. 2018, A&A, 617, A110
Pepe, F., Mayor, M., Galland, F., et al. 2002, A&A, 388, 632
Pepe, F. A., Cristiani, S., Rebolo Lopez, R., et al. 2010, Proc. SPIE, 7735, 77350F
Pepe, F., Cristiani, S., Rebolo, R., et al. 2021, A&A, 645, A96
Plez, B. 1998, A&A, 337, 495
Plez, B. 2003, ASP Conf. Ser., 298, 189
Plez, B. 2012, Astrophysics Source Code Library [record ascl:1205.004]
Press, W. H., Teukolsky, S. A., Vetterling, W. T., & Flannery, B. P. 2002, Numerical recipes in C++ : the art of scientific computing (Cambridge: Cambridge University Press)
Quirrenbach, A., Amado, P. J., Caballero, J. A., et al. 2016, Proc. SPIE, 9908, 990812
Rando, N., Asquier, J., Corral Van Damme, C., et al. 2018, SPIE Conf. Ser., 10698, 106980K
Rauer, H., Catala, C., Aerts, C., et al. 2014, Exp. Astron., 38, 249
Redfield, S., Endl, M., Cochran, W. D., & Koesterke, L. 2008, ApJ, 673, L87
Ricker, G. R. 2014, JAAVSO, 42, 234
Ryabchikova, T., Piskunov, N., Kurucz, R. L., et al. 2015, Phys. Scr., 90, 054005
Santos, N. C., Sousa, S. G., Mortier, A., et al. 2013, A&A, 556, A150
Seidel, J. V., Ehrenreich, D., Wyttenbach, A., et al. 2019, A&A, 623, A166
Sheppard, K. B., Mandell, A. M., Tamburo, P., et al. 2017, ApJ, 850, L32
Sitnova, T. M., Mashonkina, L. I., & Ryabchikova, T. A. 2013, Astron. Lett., 39, 126
Smette, A., Sana, H., Noll, S., et al. 2015, A&A, 576, A77
Sneden, C. 1973, ApJ, 184, 839
Snellen, I. A. G., Albrecht, S., de Mooij, E. J. W., & Le Poole, R. S. 2008, A&A, 487, 357
Sousa, S. G., Santos, N. C., Mayor, M., et al. 2008, A&A, 487, 373
Sousa, S. G., Santos, N. C., Adibekyan, V., Delgado-Mena, E., & Israelian, G. 2015, A&A, 577, A67
Sousa, S. G., Adibekyan, V., Delgado-Mena, E., et al. 2018, A&A, 620, A58
Tabernero, H. M., Marfil, E., Montes, D., & González Hernández, J. I. 2019, A&A, 628, A131
Tabernero, H. M., Allende Prieto, C., Zapatero Osorio, M. R., et al. 2020, MNRAS, 498, 4222
Tinetti, G., Drossart, P., Eccleston, P., et al. 2016, SPIE, 658 667
Van Eck, S., Neyskens, P., Jorissen, A., et al. 2017, A&A, 601, A10
Virtanen, P., Gommers, R., Oliphant, T. E., et al. 2020, Nat. Methods, 17, 261
Vogt, S. S., Allen, S. L., Bigelow, B. C., et al. 1994, SPIE Conf. Ser., 2198, 362
von Essen, C., Mallonn, M., Hermansen, S., et al. 2020, A&A, 637, A76
West, R. G., Hellier, C., Almenara, J.-M., et al. 2016, A&A, 585, A126
Wildi, F., Blind, N., Reshetov, V., et al. 2017, SPIE, 321, 335
Wyttenbach, A., Ehrenreich, D., Lovis, C., Udry, S., & Pepe, F. 2015, A&A, 577, A62
Yan, F., Casasayas-Barris, N., Molaverdikhani, K., et al. 2019, A&A, 632, A69

[1] Instituto de Astrofísica e Ciências do Espaço, Universidade do Porto, CAUP, Rua das Estrelas, 4150-762 Porto, Portugal
e-mail: hugo.tabernero@astro.up.pt
[2] Centro de Astrobiología (CSIC-INTA), Carretera de Ajalvir km 4, Torrejón de Ardoz, 28850 Madrid, Spain
[3] Université de Genève, Observatoire Astronomique, 51 ch. des Maillettes, 1290 Versoix, Switzerland
[4] INAF – Osservatorio Astronomico di Brera, Via Bianchi 46, 23807 Merate, Italy
[5] Instituto de Astrofísica de Canarias (IAC), 38205 La Laguna, Tenerife, Spain
[6] Universidad de La Laguna (ULL), Departamento de Astrofísica, 38206 La Laguna, Tenerife, Spain
[7] INAF, Osservatorio Astronomico di Trieste, Via Tiepolo 11, 34143 Trieste, Italy
[8] Universität Bern, Physikalisches Institut, Siedlerstrasse 5, 3012 Bern, Switzerland
[9] European Southern Observatory, Karl-Schwarzschild-Strasse 2, 85748 Garching b. München, Germany
[10] INAF – Osservatorio Astronomico di Palermo, Piazza del Parlamento 1, 90134 Palermo, Italy
[11] Faculdade de Ciências da Universidade de Lisboa (Departamento de Física), Edifício C8, 1749-016, Lisboa, Portugal
[12] INAF – Fundación Galileo Galilei, Rambla José Ana Fernandez Pérez 7, 38712 Breña Baja, Tenerife, Spain
[13] INAF – Osservatorio Astrofisico di Torino, Via Osservatorio 20, 10025 Pino Torine, Italy
[14] Departamento de Física e Astronomia, Faculdade de Ciências, Universidade do Porto, Rua do Campo Alegre, 4169-007 Porto, Portugal
[15] Institute for Fundamental Physics (IFPU), Via Beirut, 2, 34151 Grignano TS, Italy
[16] Centro de Astrofísica da Universidade do Porto, Rua das Estrelas, 4150-762 Porto, Portugal

Appendix A: Additional material

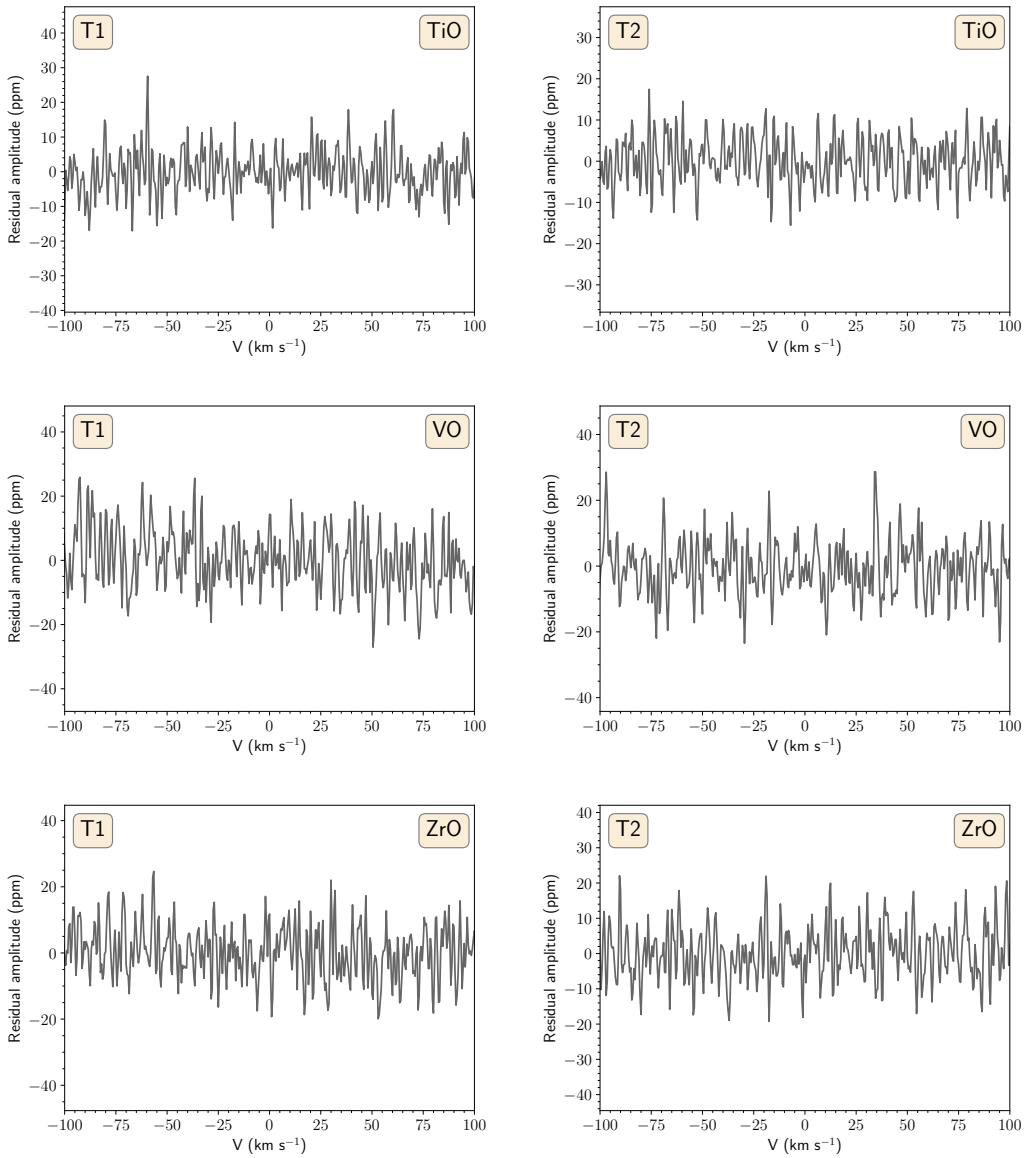

Fig. A.1. Same as Fig. 13 for diatomic molecules. *From top to bottom*: TiO, VO, and ZrO.

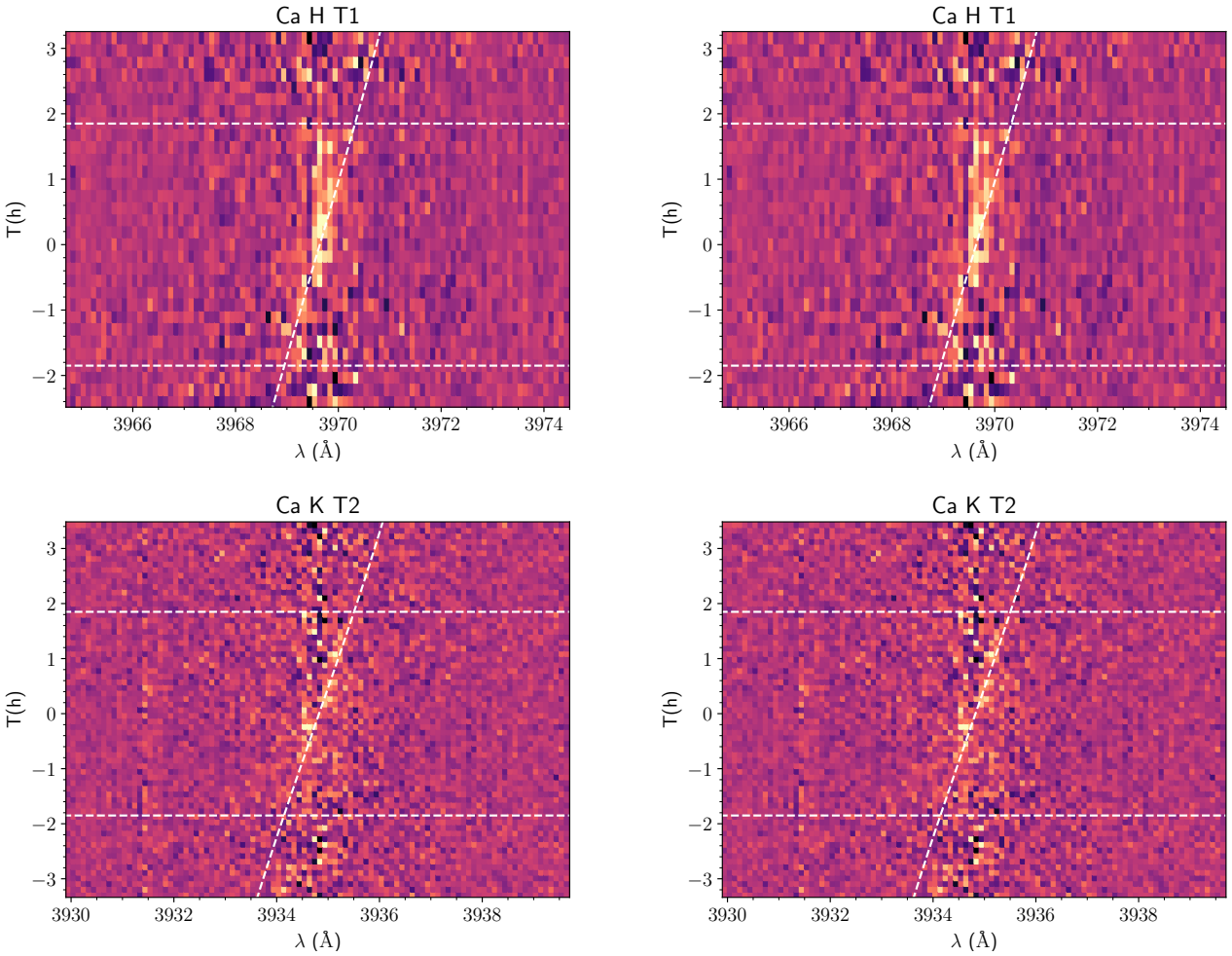

Fig. A.2. Same as Fig. 5 but for Ca II HK lines.

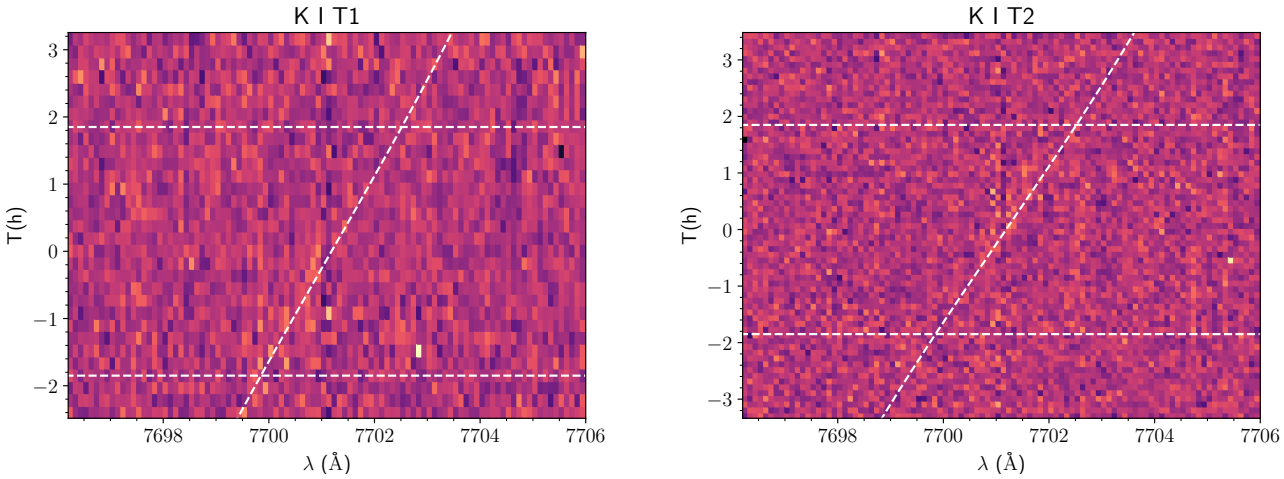

Fig. A.3. Same as Fig. 5 but for K I.

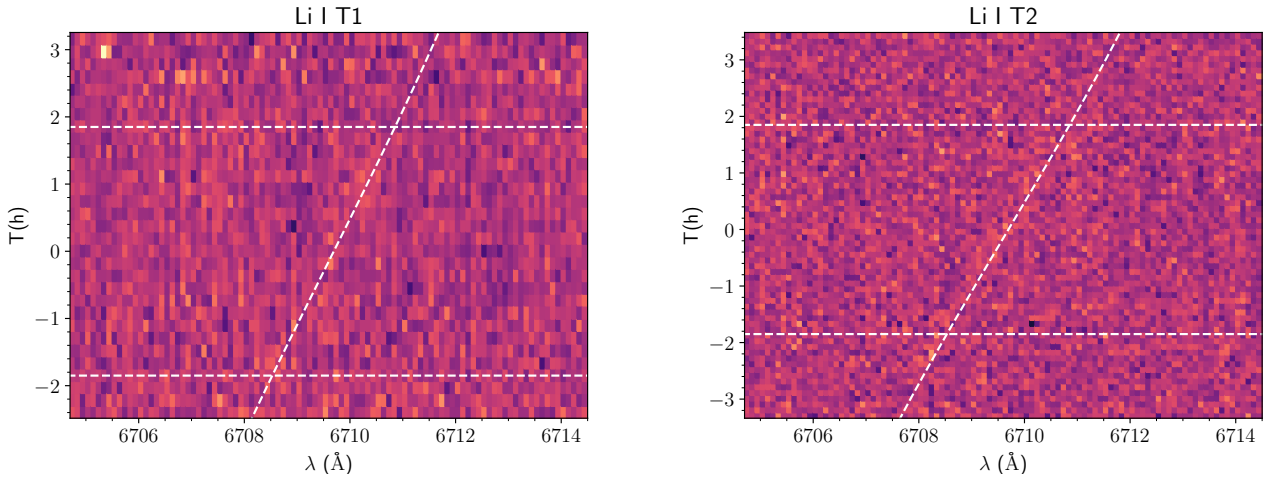

Fig. A.4. Same as Fig. 5 but for Li I.

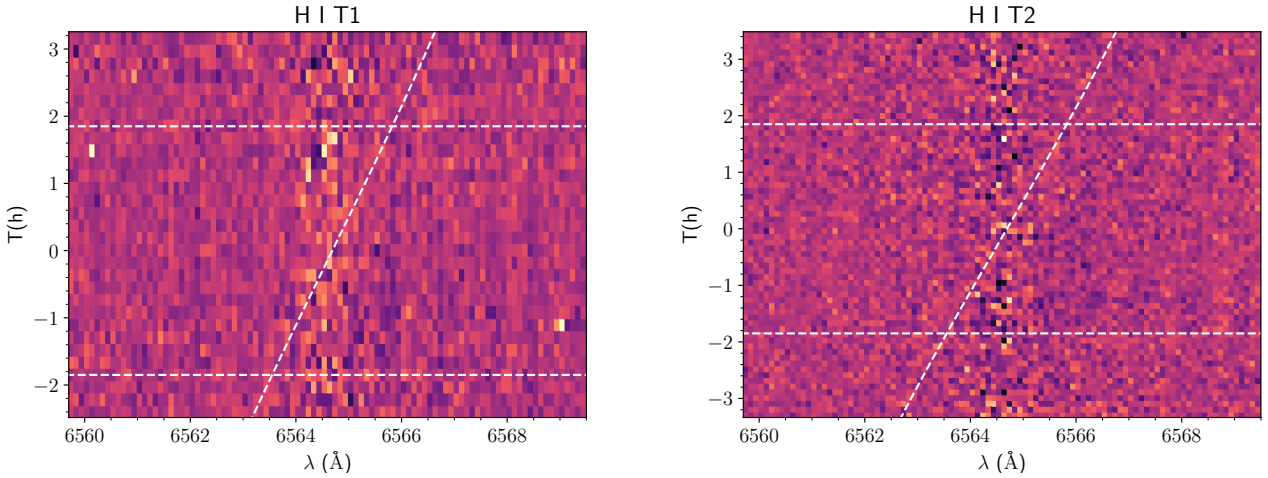

Fig. A.5. Same as Fig. 5 but for Hα.

Table A.1. Atomic data employed to calculate chemical abundances of WASP-76.

λ (Å)	Species	χ_l (eV)	$\log gf$ (dex)
6709.61	Li I	0.00	0.174
5053.55	C I	7.68	−1.304
5381.82	C I	7.68	−1.615
6589.43	C I	8.54	−1.021
7774.08	O I	9.15	0.369
7776.31	O I	9.15	0.223
7777.53	O I	9.15	0.002
6155.93	Na I	2.1	−1.547
6162.45	Na I	2.1	−1.246
5712.67	Mg I	4.35	−1.724
6320.46	Mg I	5.11	−2.103
5519.07	Si I	5.08	−2.611
5647.18	Si I	4.93	−2.043
5667.13	Si I	4.92	−1.94
5686.06	Si I	4.95	−1.553
5692.00	Si I	4.93	−1.773
5702.69	Si I	4.93	−1.953
5709.98	Si I	4.95	−1.37
5749.26	Si I	5.61	−1.543
5950.19	Si I	5.08	−1.13
6126.72	Si I	5.61	−1.464
6133.27	Si I	5.62	−1.556
6133.55	Si I	5.62	−1.615
6144.18	Si I	5.62	−1.295
6146.72	Si I	5.62	−1.31
6156.84	Si I	5.62	−0.754
6197.15	Si I	5.87	−1.49
6239.04	Si I	5.61	−0.975
6246.19	Si I	5.62	−1.093
6301.34	Si I	5.98	−1.116
6416.75	Si I	5.87	−1.035
6723.70	Si I	5.86	−1.062
6743.49	Si I	5.98	−1.653
7701.09	K I	0.0	−0.154
5263.17	Ca I	2.52	−0.579
5350.95	Ca I	2.71	−0.31
5514.51	Ca I	2.93	−0.464
5583.51	Ca I	2.52	−0.555
5591.67	Ca I	2.52	−0.571
5596.02	Ca I	2.52	0.097
5859.07	Ca I	2.93	0.24
5869.19	Ca I	2.93	−1.57
6168.15	Ca I	2.52	−1.142
6170.75	Ca I	2.52	−0.797
6171.27	Ca I	2.53	−0.478
6440.85	Ca I	2.53	0.39
6473.45	Ca I	2.53	−0.686
6495.58	Ca I	2.52	−0.109
6501.45	Ca I	2.52	−0.818
6510.65	Ca I	2.53	−2.408
6574.59	Ca I	0.0	−4.24
6719.54	Ca I	2.71	−0.524
4821.76	Ti I	1.5	−0.380
4914.98	Ti I	1.87	0.220
4979.58	Ti I	1.97	−0.303
5000.9	Ti I	0.83	0.320
5017.56	Ti I	0.85	−0.480
5024.27	Ti I	0.83	−0.330
5026.25	Ti I	0.82	−0.530
5211.83	Ti I	0.05	−0.820
5221.16	Ti I	0.02	−2.220
5691.04	Ti I	2.30	−0.360
5868.08	Ti I	1.07	−0.790
5920.18	Ti I	1.07	−1.640
5923.75	Ti I	1.05	−1.380
5980.2	Ti I	1.87	−0.440
6092.86	Ti I	2.27	−0.320
6127.91	Ti I	1.07	−1.368
6259.83	Ti I	1.44	−0.390
6262.83	Ti I	1.43	−0.530
5201.62	Cr I	3.38	−0.580
5240.42	Cr I	2.71	−1.270
5298.16	Cr I	0.98	−1.360
5299.49	Cr I	2.90	0.099
5299.75	Cr I	0.98	−1.140
5302.22	Cr I	0.98	−2.000
5305.66	Cr I	3.46	−0.670
5349.8	Cr I	1.00	−1.210
5703.89	Cr I	3.45	−0.670
6331.84	Cr I	0.94	−2.787
6015.16	Mn I	3.07	−0.354
6018.31	Mn I	3.07	−0.181
6023.46	Mn I	3.08	−0.054
4813.33	Ni I	3.66	−1.450
4905.78	Ni I	3.54	−0.016
4915.34	Ni I	3.74	−0.500
4937.21	Ni I	3.94	−0.213
4947.41	Ni I	3.80	−1.151
4954.58	Ni I	3.74	−0.580
5034.13	Ni I	3.90	−1.398
5083.76	Ni I	3.66	−0.439
5198.61	Ni I	3.90	−1.291
5437.37	Ni I	1.99	−2.580
5580.27	Ni I	1.68	−2.830
5595.29	Ni I	3.90	−0.682
5643.45	Ni I	4.11	−1.046
5696.56	Ni I	4.09	−0.467
5749.95	Ni I	1.68	−3.240
5848.61	Ni I	1.68	−3.460
6087.97	Ni I	4.27	−0.410
6109.81	Ni I	1.68	−2.600
6112.76	Ni I	4.09	−0.865
6177.08	Ni I	4.09	−0.389
6178.52	Ni I	4.09	−0.260
6188.42	Ni I	4.11	−0.880
6206.32	Ni I	4.09	−1.080
6225.7	Ni I	4.11	−0.910
6323.91	Ni I	4.15	−1.115
6329.35	Ni I	1.68	−3.170
6484.59	Ni I	1.94	−2.630
6588.13	Ni I	1.95	−2.780
6600.42	Ni I	4.24	−0.821
6636.96	Ni I	4.42	−0.765
6645.46	Ni I	1.68	−2.220
6769.64	Ni I	1.83	−2.140
6774.18	Ni I	3.66	−0.797

Table A.1. continued.